Imaging the spin chirality of ferrimagnetic Néel skyrmions stabilized on topological antiferromagnetic math xmlns="http://www.w3.org/1998/Math/MathML">mrow>msub>mi>Mn/mi>mn>3/mn>/msub>mi>Sn/mi>/mrow>/math>

Teng Xu, Zhen Chen, Heng-An Zhou, Zidong Wang, Yiqing Dong, Lucia Aballe, Michael Foerster, Pierluigi Gargiani, Manuel Valvidares, David M. Bracher, Tatiana Savchenko, Armin Kleibert, Riccardo Tomasello, Giovanni Finocchio, Soong-Guen Je, Mi-Young Im, David A. Muller, and Wanjun Jiang

Phys. Rev. Materials **5**, 084406 — Published 13 August 2021

DOI: 10.1103/PhysRevMaterials.5.084406

Imaging the spin chirality of ferrimagnetic Néel skyrmions stabilized on topological antiferromagnetic Mn_3Sn

Teng Xu[1,2,*], Zhen Chen[3,4,*], Heng-An Zhou[1,2], Zidong Wang[1,2], Yiqing Dong[1,2], Lucia Aballe[5], Michael Foerster[5], Pierluigi Gargiani[5], Manuel Valvidares[5], David M. Bracher[6], Tatiana Savchenko[6], Armin Kleibert[6], Riccardo Tomasello[7], Giovanni Finocchio[8], Soong-Guen Je[9], Mi-Young Im[9], David A. Muller[3,4,†] and Wanjun Jiang[1,2,†]

[1]*State Key Laboratory of Low-Dimensional Quantum Physics and Department of Physics, and Tsinghua University, Beijing 100084, China*

[2]*Frontier Science Center for Quantum Information, Tsinghua University, Beijing 100084, China*

[3]*School of Applied and Engineering Physics, Cornell University, Ithaca, NY 14853, USA*

[4]*Kavli Institute at Cornell for Nanoscale Science, Cornell University, Ithaca, NY 14853, USA*

[5]*ALBA Synchrotron Light Source, Cerdanyola del Vallès, 08290 Barcelona, Spain*

[6]*Paul Scherrer Institut, 5232 Villigen PSI, Switzerland*

[7]*Institute of Applied and Computational Mathematics, FORTH, GR-70013, Heraklion-Crete, Greece*

[8]*Department of Mathematical and Computer Sciences, Physical Sciences and Earth Sciences, University of Messina, Messina 98166, Italy*

[9]*Center for X-ray Optics, Advanced Light Source, Lawrence Berkeley National Laboratory, Cyclotron Road, Berkeley, CA 94720, USA*

[*]These authors contributed equally.

[†]Correspondences should be addressed to:

David.a.muller@cornell.edu

jiang_lab@tsinghua.edu.cn

ABSTRACT

Néel skyrmions are generally realized in asymmetric multilayers made of heavy metals and ultrathin ferromagnets possessing strong interfacial Dzyaloshinskii-Moriya interactions (iDMI). Depending on the relative strengths of iDMI at the interfaces, various types of Néel skyrmions have been suggested, which are typified with characteristically different topological properties and current-driven dynamics. This suggests the importance of a precise quantification of their spin chiralities. In this study, we will first explore the possibility of realizing Néel skyrmions in magnetic multilayers without the direct usage of standard heavy metals. Specifically, through depositing a thin layer of ferrimagnetic (FIM) CoTb layer on top of an antiferromagnetic (AFM) quantum material of composition Mn_3Sn, the AFM exchange interaction at the asymmetric interface provides an equivalent iDMI for stabilizing FIM Néel skyrmions. Secondly, through using the advanced four-dimensional Lorentz scanning transmission electron microscopy (4D LSTEM), in combination with the X-ray magnetic circular dichroism - photoemission electron microscopy (XMCD-PEEM), we are able to directly determine the spin chirality of FIM Néel skyrmions. The present findings not only broaden the phase space for chiral interfacial magnetism but also provide a possibility for future applications of heavy-metal-free skyrmionic devices.

I. INTRODUCTION

Magnetic skyrmions are noncollinear topological spin textures that have been extensively studied in bulk magnets[1-3] and magnetic multilayers[4,5]. For potential spintronic applications, interfacially asymmetric multilayers of stacking order heavy $metal_1$/ultrathin ferromagnet/heavy $metal_2$ (HM_1/FM/HM_2), where HM_2 can be either a different material or implying a different interface characteristic due to growth, are particularly promising for hosting room-temperature Néel skyrmions[6-19]. In these multilayers, standard HM layers (such as Pt, Ta, W, Ir and Pd) or topological insulators (TIs) with strong spin-orbit couplings (SOCs) are generally required for mediating the iDMI that subsequently determines the spin chirality of Néel-type spin textures[20-28].

In this regard, it is important to explore alternative Néel-skyrmion-hosting multilayers without directly involving the standard HM layers. In particular, Néel-type chiral spin textures stabilized on top of quantum materials with a relatively weak SOC, such as topological antiferromagnet Mn_3Sn in the present study, have not been studied. Such investigations could broaden the material choice of Néel skyrmions and greatly contribute to the current understandings of chiral interfacial magnetism[29,30]. Note that Bloch-type skyrmions have been observed in non-centrosymmetric bulk magnets such as MnSi, FeGe, in which spins rotate spirally that is different with the cycloidal rotation of spins in Néel-type skyrmions[31].

Another challenging topic is the direct imaging of the spin chirality of Néel skyrmions at room temperature. One of the most frequently used high-resolution techniques is the Lorentz transmission electron microscopy (LTEM)[3,13,32,33]. It worth mentioning that Néel skyrmions stabilized by the iDMI exhibit a uniform spin chirality[34,35], while Bloch-type magnetic bubbles stabilized by the dipole interactions exhibit random spin topologies over the entire films[36,37]. It has been demonstrated that Néel skyrmions and Bloch-type bubbles show distinctively different contrasts at tilted conditions in LTEM images[38]. In the perpendicularly magnetized multilayers, the long-range dipolar interaction would preferentially form Bloch-type spin textures, while the iDMI would stabilize the Néel-type spin textures. Meanwhile, through detecting the tilt-dependent magnetic contrast, the LTEM technique can conclusively distinguish Néel from Bloch skyrmions[13,39-41]. However, the in-plane components (spin chirality) of Néel skyrmions exhibit subtle contributions to the LTEM images and their effects cannot be convincingly extracted[13,32,33,39-41].

We will show here that the spin chirality of Néel skyrmions could be determined by using an advanced four-dimensional Lorentz scanning TEM (4D LSTEM), a determination which is not accessible in conventional Lorentz TEM. Our 4D LSTEM instrument is equipped with a high-dynamic-range electron microscopy pixel array

detector (EMPAD)[40,42], which enables quantitative spin-texture imaging in embedded magnetic multilayers with a spatial resolution of a few nanometers towards atomic resolution. It is also capable to add various external stimuli in the LSTEM setup, such as current, voltage, and magnetic field (along the beam direction) in a wide temperature range. It should be mentioned here that the chiral nature of FIM Néel skyrmions is, however, not directly revealed due to the technical limitations of different electron microscopes[22,43-46]. Additionally, a table for comparing different imaging techniques is given in the Part 1 of Supplementary Materials[47]. Combined with the XMCD-PEEM imaging, we can further identify the antiparallel spin configurations of the sublattices of the FIM Néel skyrmion.

In this study, we use one of the representative quantum materials, the noncollinear topological AFM Mn_3Sn to replace the frequently utilized HM layers and to experimentally demonstrate the stabilization of Néel skyrmions at room temperature. Mn_3Sn exhibits a noncollinear triangular AFM spin configuration with a vanishing net magnetic moment[48,49], as shown in Fig. 1A. Recently, a large anomalous Hall effect, a large anomalous Nernst effect, a large magnetic-optical effect, a magnetic spin Hall effect and magnetic Weyl fermions have been observed in this noncollinear antiferromagnet[50-53]. These intriguing observations thus signify Mn_3Sn as one of the representative quantum materials. Further, theoretical investigations have predicted a very weak spin-orbit coupling in the intrinsic noncollinear AFM Mn_3Sn and their chiral magnetism[54-56]. In adjacent to magnetic layers (ferrimagnetic CoTb in our case), the interfacial chiral magnetism can be expected to be established at the surface of Mn_3Sn through the interlayer exchange coupling.

Interestingly, recent theoretical calculations have predicted that the triangular spin arrangement of the Mn sites possesses an iDMI of non-relativistic origin[57]. Thus, the naturally existing iDMI in Mn_3Sn could be harvested for stabilizing chiral spin structures in Mn_3Sn/FM bilayers. The feasibility of this proposal has been theoretically

suggested through studying the interface between $L1_2$-type Mn_3Ir and Co (111), in which a substantial iDMI strength has been suggested through *ab initio* calculations[58]. Note that $L1_2$-type Mn_3Ir and Mn_3Sn are both noncollinear AFMs with the same triangular AFM spin arrangements[59]. Therefore, the iDMI with the same origin may also exist in the FIM/Mn_3Sn bilayer. This theoretical prediction partly motivates the present experimental studies.

II. MATERIALS AND METHODS

Mn_3Sn thin films, possessing hexagonal Ni_3Sn-type structure with space group P63/mmc, were fabricated on the Al_2O_3 single crystalline and thermally oxidized silicon substrates by AJA (Orion 8) ultrahigh vacuum magnetron sputtering system. In the meanwhile, $[Mn_3Sn(3)/Co_{75}Tb_{25}(6)/Si_3N_4(2.9)]_{20}$ and $[Si_3N_4(2.9)/Co_{75}Tb_{25}(6)/Mn_3Sn(3)]_{20}$ (thickness in nanometer) magnetic multilayers were also deposited. The base pressure of the growth chamber is 2.0×10^{-8} Torr and the Ar working pressure was maintained at 3.0 mTorr during film deposition. The deposition rate of Mn_3Sn is 0.6 Å/s. The 6 nm-thick CoTb layers with bulk perpendicular magnetic anisotropy (PMA) were prepared in a co-sputtering mode, with their relative concentrations being adjusted by changing the relative growth powers. Magnetic multilayers were also deposited on the 100 nm- and 15 nm-thick Si_3N_4 membranes for magnetic imaging using the soft X-ray microscopy (XM-1) and LTEM, respectively. The same multilayer were also grown on thermally oxidized silicon substrates for magnetic characterization and XMCD-PEEM imaging. The electronic transport properties of the samples were measured by using a physical property measurement system (PPMS, Quantum Design). The magnetic properties of the Mn_3Sn films and multilayers were studied by using a superconductor quantum interference device (SQUID) magnetometer (MPMS, Quantum Design). The magnetic imaging is conducted at Co L_3 edge (778.5 eV) by using a full-field magnetic transmission X-ray microscopy (MTXM) performed at Advanced Light Source (ALS). The X-ray absorption spectroscopy (XAS) and X-ray magnetic circular dichroism (XMCD)

measurements were conducted at the Co and Mn $L_{2,3}$ and the Tb $M_{4,5}$ edges, respectively. The XMCD-PEEM experiments were performed at Paul Scherrer Institute PSI and ALBA Synchrotron Light Source.

III. RESULTS AND DISCUSSION

Fig. 1B shows the room temperature hysteresis loops ($M - H_z$) measured with a perpendicular magnetic field (H_z) for Mn_3Sn films grown on top of $[1\bar{1}02]$-orientated Al_2O_3 substrate. A saturation magnetization $M_s = 1.2 \times 10^4$ A/m is estimated which is expected due to the noncollinear AFM order in Mn_3Sn. The Mn atoms form a slightly distorted kagome lattice and the associated geometrical frustration manifests itself as an inverse triangular spin structure, which gives rise to a weak magnetic moments[60,61]. The resulting small net magnetization thus allows the field-control of noncollinear antiferromagnetism in Mn_3Sn and more importantly, its electrical detection by the anomalous Hall effect[49]. Similar with the occurrence of the giant anomalous Hall effect (AHE) in the Mn_3Sn single crystal, a giant AHE is observed and shown in Fig. 1C. Note that these samples were grown simultaneously on Al_2O_3 and SiO_2 substrates. The occurrence of the giant AHE in both samples thus implies the presence of topological noncollinear spin configuration. Note that the amplitude of AHE in Mn_3Sn/SiO_2 is smaller than that of Mn_3Sn/Al_2O_3, indicating a smaller portion of Mn_3Sn grains exhibit triangular spin configuration. A 6 nm-thick $Co_{75}Tb_{25}$ layer is subsequently deposited on top of Mn_3Sn. The presence of PMA is confirmed by the AHE measurement, which only probes the magnetization orientation of Co (M_{Co}), as a result of the weak coupling between the conduction electron spins and magnetic moments of Tb (M_{Tb})[62]. The magnetization of Tb (parallel with external field) is opposite with that of Co (antiparallel with external field), due to the AFM coupling between the Co and Tb sublattices[62]. After inserting a thin layer of Ti (1 nm) between Mn_3Sn and $Co_{75}Tb_{25}$, it is evident that the shape of AHE loop is strongly modulated, as shown in Fig. 1D. Together with the large coercive field and saturation field, the modulated AHE loops suggest the existence of an interlayer AFM exchange coupling

between Mn_3Sn and $Co_{75}Tb_{25}$ films.

The opposite stacking order, $[Mn_3Sn/Co_{75}Tb_{25}/Si_3N_4]_{20}$ and $[Si_3N_4/Co_{75}Tb_{25}/Mn_3Sn]_{20}$, is expected to provide a flipped sign for the iDMI and hence an opposite spin chirality, as schematically shown in Fig. 2A. The layer-resolved film growth of multilayers and layer thickness can be determined from a cross-sectional STEM image, as shown in Fig. 2B. Layered structures are further verified by the elemental mapping from the electron energy loss spectroscopy for both films, as shown in Part 2 of Supplementary Materials[47]. Note that the O-K edge overlaps with the Sn M edge, adding a small offset to the intensity of the Sn profile in EELS as a consequence of the inclusion of oxygen from the surface oxidation during TEM specimen preparation and should not be considered as an intermixing between the Sn-containing and other layers. $M - H_z$ loop measured with the perpendicular magnetic field (H_z) is shown in Fig. 2C. The shape of which is similar to typical Néel-skyrmion-hosting multilayers such as $[Pt/CoFeB/MgO]_{15}$, and $[Pt/Co/Ir]_{15}$, implying the possible formation of Néel skyrmions in our systems[7,8]. The (small) net saturation magnetization $M_s = M_{Tb} - M_{Co} = 1.9 \times 10^5\ A/m$ can be attributed to the partially compensated magnetism between the Tb and Co sublattices that gives rise to the formation of FIM Néel skyrmions[12]. Shown in Fig. 2D is the hysteresis loop measured in the sample plane (H_x), from which the anisotropy field $H_k \sim 6000$ Oe can be estimated.

Magnetic imaging in the $[Mn_3Sn/Co_{75}Tb_{25}/Si_3N_4]_{20}$ multilayer is first performed using the soft X-ray transmission microscopy (XM-1) with a spatial resolution down to 20 nm at the Co L_3 edge (778.5 eV). Following the increase of $\mu_0 H_z$, disordered labyrinthine domains gradually shrink into isolated bubble-like spin textures, which occurs from the competition between the exchange interaction, magnetic anisotropy, dipole-dipole interaction and the (effective) iDMI, as confirmed by our micromagnetic simulations. A detailed examination of the magnetic domain configurations as a function of $\mu_0 H_z$ is presented in Fig. S3 of Part 3 of Supplementary Materials[47]. Fig.

2E shows a selected image acquired at $\mu_0 H_z = 141$ mT, in which sparsely distributed bubble-like spin textures can be found. Through using a 360 degree domain wall (DW) model[43], the diameter of these bubbles is determined to be in the range of 90 nm – 200 nm, which is larger than the resolution of X-ray transmission microscope (20 nm). Note that XM-1 probes only the out-of-plane magnetization component ($m_{z/\mathrm{Co}}$) of the Co element, as a result of the normal incidence of the soft X-ray to specimens. The missing information on the orientation of the in-plane magnetization component ($m_{x,y/\mathrm{Co}}$ and $m_{x,y/\mathrm{Tb}}$) is, however, extremely vital for quantifying the spin-chirality of FIM Néel skyrmions as shown below.

The size evolution of these bubble-like spin textures as a function of $\mu_0 H_z$ is further summarized in Fig. 2F. Following the increase of $\mu_0 H_z$, the diameter of bubbles is monotonically decreasing. Based on the material specific parameters, micromagnetic simulations are carried out using two coupled Landau-Lifshitz-Gilbert equations[63,64]. The $Co_{75}Tb_{25}$ ferrimagnet with two sublattices composed of Co and Tb was considered. Note that a similar value of effective exchange A = 15 pJ/m for similar FIMs is reported in earlier works[62,65-67]. We analyze a 500 × 500 nm^2 squared sample with a thickness of 6 nm. A detailed description can be found in Part 4 of Supplementary Materials[47]. Using an effective iDMI parameter $D_i = 1.5 \pm 0.1$ mJ/m^2, it can be seen that the micromagnetic simulation largely reproduces the experimental data. This consistency has also been verified by multilayer simulations (20 repetitions), and thus suggests a semi-quantitative estimation of a finite iDMI in the present multilayer.

Through detecting the phase shift of the electron beam induced by the lateral magnetic induction field ($B_{x,y}$) in magnetic samples, LTEM has been frequently used to map out the profile of different types of spin textures[3,32]. In standard Lorentz mode with a normal incidence of electron beam, there is, however, no visible magnetic contrasts for Néel-type spin textures, due to the absence of lateral magnetic induction. Tilting samples away from the normal incidence introduces magnetic contrasts, mainly

originating from the lateral projection of the out-of-plane components of the magnetization (m_z)[13,32,33]. Such a tilt-dependent magnetic contrast has been widely used to distinguish Néel from Bloch DWs and skyrmions[13,39-41]. At zero field, overfocused LTEM images are acquired for the $[Mn_3Sn/Co_{75}Tb_{25}/Si_3N_4]_{20}$ multilayer, under a tilting angle from plane normal of -20°, 0, and 20°, as shown in Figs. 3A-3C. In standard Lorentz mode, the external field is applied along the electron beam direction. Sparsely distributed bubble-like spin textures at 104 mT with a tilting angle 20° is also shown in Fig. 3D. Shown in Figs. 3E-3H are the corresponding LTEM images acquired in the inverted stack $[Si_3N_4/CoTb/Mn_3Sn]_{20}$. At the zero tilting angle, a diminishing magnetic contrast is evident in both samples. Through reversing the tilting angle from -20° to 20°, a reversal of magnetic contrast can also be seen. The reversal of bubble-like magnetic contrast at 104 mT, which is obtained at opposite tilting angles (-20° and 20°), is also demonstrated in Part 5 of Supplementary Materials[47]. These results are consistent with the reported LTEM images of Néel-type spin textures. However, the in-plane components of the Néel-type spin textures ($m_{x,y}$) have a subtle contribution to the LTEM images and their effects cannot be extracted due to the challenges for quantifying the images[32,33]. Therefore, the spin chirality of these Néel skyrmions cannot be directly determined from the standard LTEM images[13,32,33,39-41].

Differential phase contrast (DPC) imaging in LSTEM mode using a focused electron probe can directly measure the deflection angle of the electron beam ($\beta_L = \frac{e\lambda}{h} B_{x,y} t$) induced by the Lorentz force of the lateral magnetic field ($B_{x,y}$) in the sample with the possibility of reaching atomic resolution[68]. Here e is the unitary electronic charge, λ is the wavelength of the electron beam, h is the Planck constant and t is the thickness of the magnetic film. It provides the capabilities for quantitatively imaging the spin structures at a sub-5 nm spatial resolution, which are usually inaccessible from LTEM. In particular, the resolution of LTEM degrades to tens of nanometers due to the delocalization from the large defocus value required for gaining sufficient magnetic contrast[39], especially for compensated FIMs with a small saturation magnetization.

This is not a problem for LSTEM for which is operated in focus. High sensitivity to magnetic field from LSTEM relies on more illumination doses and therefore a high dynamic range detector. Fig. 4A shows schematically our LSTEM setup equipped with a high-dynamic-range electron microscopy pixel array detector (EMPAD). A 4D dataset is obtained by acquiring the full diffraction pattern at each scanning point. Compared with conventional DPC imaging, the 4D LSTEM setup can determine the deflection angle of the electron beam more accurately from the diffraction patterns via a more advanced analysis such as an edge detection algorithm[40]. These analyses can largely eliminate the artifacts from crystalline grains that are unavoidable in the sputtered polycrystalline or amorphous films[42]. Here, we will show that 4D LSTEM can be utilized to directly visualize the spin chirality of the Néel skyrmions.

Employing a 360° DW model[43] and following the established theory of Lorentz electron microscopy[69], we can simulate the magnetic induction field from Néel skyrmions with an opposite spin chirality. Panels R2 & L2 in Fig. 4B and 4C shows simulated magnetic induction fields along the horizontal direction (B_x) for a right-handed (Panel R1) and a left-handed (Panel L1) spin chirality of Néel skyrmions. The black curves in Panels R3 & L3 show an asymmetric feature along the simulated diagonal direction (B_x) for the right-handed and the left-handed spin chiralities, respectively. As illustrated from the separate contributions of the in-plane ($m_{x,y}$) and out-of-plane (m_z) magnetization components in Fig. S5 of Part 6 of Supplementary Materials[47], the reversal of the asymmetric intensity comes from the reversed spin orientation of the in-plane components ($m_{x,y}$). This can thus be used to directly identify the spin chiralities of Néel skyrmions. Subtle asymmetric features can also be seen in vertical component (B_y) and the magnitude ($|\boldsymbol{B}| = \sqrt{B_x^2 + B_y^2}$), as shown in Fig. S6 of Part 7 of Supplementary Materials[47]. Our quantitatively calculated magnetic induction fields thus suggest that 4D LSTEM can be used for mapping out the spin chirality of Néel skyrmions.

Panels R4 & L4 show the experimentally acquired magnetic flux (B_x) images using 4D LSTEM. The selected right- and left-handed Néel skyrmion (red circles in Panels R4 &L4) is shown in the panel R5 and L5, which were acquired from the $[Mn_3Sn/Co_{75}Tb_{25}/Si_3N_4]_{20}$ and $[Si_3N_4/CoTb/Mn_3Sn]_{20}$ multilayers with flipped surfaces, respectively. The red curves in Panels R3 & L3 show their line profiles along the diagonal directions of experimental magnetic flux B_x. The asymmetric features qualitatively agree with the simulated results, as shown in Panels R3 & L3. A small residual offset in the zero point of magnetic field may exist from LSTEM measurements. Because the zero-field point was calibrated by zeroing the beam deflection angle from sample regions far from skyrmions and without apparent magnetic contrast. The possible long-range field from skyrmions can induce a small shift in the magnetic field. The overall shape of the vertical direction (B_y) and magnitude ($|B|$) of the magnetic induction field images also qualitatively agrees with the simulations, as shown in Part 8 of Supplementary Materials[47]. Thus, the spin chirality of Néel skyrmions, being the right-handed or left-handed in these two inverted multilayers, was confirmed. Note that the right-handed and left-handed spin chiralities correspond to positive and negative signs of the iDMI parameters respectively, which is expected for the inverted stacking orders[70]. We also find that local sample bending or crystalline grains may introduce artifacts into the magnetic flux images, which were carefully avoided during our experiments. Furthermore, the signal-to-noise ratio of the magnetic field images scales with the exposure dose, requiring a high dynamic range detector like the EMPAD for identifying the spin chirality of Néel skyrmions[42,71].

We also note that the shape or size of magnetic flux distribution from Néel skyrmions can be affected by many factors, such as local defects pinning or residual magnetic field from neighboring Néel skyrmions. In our experiments, we chose Néel skyrmions without apparent distortions. Line profiles of magnetic field from both B_x and B_y components of more undistorted Néel skyrmions are further shown in Panels R6 and

L6 in the Fig. 4 and Fig. S8 in the Part 9 of Supplementary Materials[47], respectively. It is worth mentioning that the small in-plane external magnetic field (< 50 mT) is much smaller than those of the effective field of the interfacial DMI and should have negligible effects on the identification of the chirality in the films. Note that 4D LSTEM experiment is also performed in $[Si_3N_4/Co_{0.75}Tb_{0.25}]_{20}$ multilayers, in which the presence of Bloch-type spin textures is identified, as illustrated in Part 10 of Supplementary Materials[47]. We also notice that Bloch-type bubbles with random spin topology are recently reported in the very thick CoTb film without an interfacial asymmetry[72]. These results further suggest the important role of noncollinear AFM Mn_3Sn in introducing interfacial chiral magnetism.

The incorporation of FIM $Co_{75}Tb_{25}$ layer with two AFM-coupled Tb and Co sublattices results in the formation of FIM Néel skyrmions. The 4D LSTEM measurement is, however, only sensitive to the net magnetization ($|M_{\mathrm{Tb}} - M_{\mathrm{Co}}|$). In order to confirm the presence of FIM Néel skyrmions and their associated (opposite) spin chiralities in an element-specific measurement, we also performed XMCD spectroscopy and XMCD-PEEM experiments, as shown in Fig. 5. Measuring Co $L_{2,3}$ and Tb $M_{4,5}$ absorption edges XMCD spectra at $\mu_0 H_{\mathrm{z}} = 2\ \mathrm{T}$, opposite signs are evident, corresponding to the antiparallel magnetization of Co and Tb atoms. Note that the vanishing XMCD signals at Mn $L_{2,3}$ absorption edge can be observed, which exclude the proximity-induced magnetism in Mn_3Sn, as shown in Fig. S10 of Part 11 of Supplementary Materials[47]. Insets of Figs. 5A and 5B show XMCD-PEEM images of an identical area acquired at the Co L_3 and Tb M_5 edges at zero magnetic field, respectively. The reversed magnetic contrasts between these two images further confirm the AFM coupling between the Tb and Co sublattices.

In the XCMD-PEEM investigations, the samples are illuminated with the X-ray beam at a small grazing angle (typically 16°) with respect to the film plane. Hence, the magnetic contrast of the in-plane magnetization component ($m_{x,y}$) is about 3.5 times

stronger than that of the out-of-plane components (m_z)[24]. Specifically, the change of magnetic contrast correlates with the relative orientation between the in-plane magnetization and the X-ray incidence direction. The contrast is bright when the in-plane magnetization is antiparallel with the X-ray incidence direction, whereas a dark contrast is present when they are in a parallel configuration. Thus, together with its high spatial resolution (possibly down to 25 nm), XMCD-PEEM can be independently employed for confirming the spin chirality of Néel-type spin textures.

Fig. 5C displays a high-resolution XMCD-PEEM image of the multidomain states at zero field for $[Mn_3Sn/CoTb/Si_3N_4]_{20}$ multilayer acquired at the Tb M_5 edge. Along the X-ray illumination direction, an alternating contrast change from brighter to darker can be observed, which corresponds to the down-to-up (↓↙←↖↑) DW and up-to-down (↑↗→↘↓) DW, respectively. These features can be more clearly seen from the linescan shown in Fig. 5D, which confirms that the spin chirality in the $[Mn_3Sn/CoTb/Si_3N_4]_{20}$ multilayer is right-handed. Experimental efforts are also made to directly image the spin chirality of Co at L_3 edge, which is however unsuccessful due to a relatively smaller magnetization and hence a weaker XMCD-PEEM contrast. As a result of AFM coupling between the Tb and Co sublattices, the Co sublattice possesses the same spin chirality as Tb sublattice, as schematically illustrated in the inset of Fig. 5D.

IV. CONCLUSIONS

In summary, using the noncollinear AFM Mn_3Sn as a seeding layer and the accompanied interfacial AFM exchange coupling through interfacing with a thin FIM CoTb layer, we have stabilized FIM Néel skyrmions in $[Mn_3Sn/CoTb/Si_3N_4]_{20}$ and $[Si_3N_4/CoTb/Mn_3Sn]_{20}$ multilayers, respectively. The opposite (right/left-handed) spin chirality due to the flipped interfaces and hence the opposite (positive/negative) sign of the iDMI can be directly identified by using the 4D LSTEM, in combination with the imaging simulations. The 4D LSTEM results, together with FIM nature of the Néel skyrmions in our multilayers are further confirmed using XMCD-PEEM. Our results

suggest that the exchange coupling between a noncollinear AFM and a thin FIM could similarly host an iDMI of strength 1.5 ± 0.1 mJ/m^2 that can be harvested to stabilize room-temperature Néel skyrmions. Meanwhile, it is interesting to note that a negative sign of the iDMI parameter has been measured in IrMn/CoFeB/MgO trilayers[73-75], as compared with the positive sign of the iDMI in the Mn_3Sn/CoTb/Si_3N_4 multilayer. Thus, a precise understanding of the rich interfacial chiral magnetism in similar AFM-based quantum materials, however, requires further theoretical investigations, ideally from the first principle calculation and ab initio calculations[76]. We also summarized different skyrmion hosting materials in a table in Part 12 of Supplementary Materials[47], which could be beneficial for the future material optimization. Compared to the other materials, the choice of FIM CoTb with a bulk PMA could stimulate more applications of quantum materials in chiral magnetism. Furthermore, one could envision to harvest the accompanied magnetic spin Hall effects from the topological Mn_3Sn in order to study the current-driven dynamics of FIM Néel skyrmions[52,59,77], which may simultaneously reveal interesting physics such as the reduced skyrmion Hall effect. In the meanwhile, one could explore the intralayer exchange between the skyrmion hosting multilayers and Mn_3Sn, for stabilizing AFM skyrmions. It is expected that the present work could trigger more intense investigations for gaining a comprehensive understanding of chiral interfacial magnetism and meanwhile, could set a valuable step for bridging AFM spintronics and skyrmionics in the future[78,79].

ACKNOWLEDGEMENTS

Work carried out at Tsinghua was supported by the National Key R&D Program of China (Grant No. 2017YFA0206200), Basic Science Center Project of NSFC (Grant No. 51788104), National Key R&D Program of China (Grant No. 2016YFA0302300), the National Natural Science Foundation of China (Grant No. 11774194, 51831005, 1181101082, 11804182), Beijing Natural Science Foundation (Grant No. Z190009), Tsinghua University Initiative Scientific Research Program and the Beijing Advanced

Innovation Center for Future Chip (ICFC). Electron microscopy at Cornell University was supported by U.S. DARPA (TEE-D18AC00009) and U.S. PARADIM NSF Materials Innovation Platform (DMR-1539918). Electron microscopy facilities at Cornell supported by the Cornell Center for Materials Research, an NSF MRSEC (DMR-1719875). Work at the ALS were supported by U.S. Department of Energy (DE-AC02-05CH11231). Part of this work was carried out at the Surface/Interface: Microscopy beamline of the Swiss Light Source. Funding by the Swiss National Science Foundation through grant 200021-160186 and Swiss Nanoscience Institute through grant P1502 is acknowledged. M.-Y. Im acknowledges support by Lawrence Berkeley National Laboratory through the Laboratory Directed Research and Development (LDRD) Program and the National Research Foundation of Korea (NRF) grant funded by the Korea government (MSIT) (NRF-2019R1A2C2002996, NRF-2016M3D1A1027831, and NRF-2019K1A3A7A09033400). R.T. and G.F. thank the project "ThunderSKY" funded from the Hellenic Foundation for Research and Innovation (HFRI) and the General Secretariat for Research and Technology (GSRT) under Grant No. 871.

REFERENCES

[1] U. K. Rößler, A. N. Bogdanov, and C. Pfleiderer, Spontaneous skyrmion ground states in magnetic metals, Nature **442**, 797 (2006).

[2] S. Mühlbauer, B. Binz, F. Jonietz, C. Pfleiderer, A. Rosch, A. Neubauer, R. Georgii, and P. Böni, Skyrmion Lattice in a Chiral Magnet, Science **323**, 915 (2009).

[3] X. Z. Yu, Y. Onose, N. Kanazawa, J. H. Park, J. H. Han, Y. Matsui, N. Nagaosa, and Y. Tokura, Real-space observation of a two-dimensional skyrmion crystal, Nature **465**, 901 (2010).

[4] S. Heinze, K. von Bergmann, M. Menzel, J. Brede, A. Kubetzka, R. Wiesendanger, G. Bihlmayer, and S. Blügel, Spontaneous atomic-scale magnetic skyrmion lattice in two dimensions, Nat. Phys. **7**, 713 (2011).

[5] N. Romming, C. Hanneken, M. Menzel, J. E. Bickel, B. Wolter, K. von Bergmann, A. Kubetzka, and R. Wiesendanger, Writing and Deleting Single Magnetic Skyrmions, Science **341**, 636 (2013).

[6] W. Jiang, P. Upadhyaya, W. Zhang, G. Yu, M. B. Jungfleisch, F. Y. Fradin, J. E. Pearson, Y. Tserkovnyak, K. L. Wang, O. Heinonen, S. G. E. te Velthuis, and A. Hoffmann, Blowing magnetic skyrmion bubbles, Science **349**, 283 (2015).

[7] C. Moreau-Luchaire, C. Moutafis, N. Reyren, J. Sampaio, C. A. F. Vaz, N. Van

Horne, K. Bouzehouane, K. Garcia, C. Deranlot, P. Warnicke, P. Wohlhüter, J. M. George, M. Weigand, J. Raabe, V. Cros, and A. Fert, Additive interfacial chiral interaction in multilayers for stabilization of small individual skyrmions at room temperature, Nat. Nanotechnol. **11**, 444 (2016).

[8] S. Woo, K. Litzius, B. Krüger, M.-Y. Im, L. Caretta, K. Richter, M. Mann, A. Krone, R. M. Reeve, M. Weigand, P. Agrawal, I. Lemesh, M.-A. Mawass, P. Fischer, M. Kläui, and G. S. D. Beach, Observation of room-temperature magnetic skyrmions and their current-driven dynamics in ultrathin metallic ferromagnets, Nat. Mater. **15**, 501 (2016).

[9] A. Fert, N. Reyren, and V. Cros, Magnetic skyrmions: advances in physics and potential applications, Nat. Rev. Mater. **2**, 17031 (2017).

[10] W. Jiang, G. Chen, K. Liu, J. Zang, S. G. E. te Velthuis, and A. Hoffmann, Skyrmions in magnetic multilayers, Physics Reports **704**, 1 (2017).

[11] T. Yokouchi, S. Sugimoto, B. Rana, S. Seki, N. Ogawa, S. Kasai, and Y. Otani, Creation of magnetic skyrmions by surface acoustic waves, Nat. Nanotechnol. **15**, 361 (2020).

[12] S. Woo, K. M. Song, X. Zhang, Y. Zhou, M. Ezawa, X. Liu, S. Finizio, J. Raabe, N. J. Lee, S.-I. Kim, S.-Y. Park, Y. Kim, J.-Y. Kim, D. Lee, O. Lee, J. W. Choi, B.-C. Min, H. C. Koo, and J. Chang, Current-driven dynamics and inhibition of the skyrmion Hall effect of ferrimagnetic skyrmions in GdFeCo films, Nat. Commun. **9**, 959 (2018).

[13] S. D. Pollard, J. A. Garlow, J. Yu, Z. Wang, Y. Zhu, and H. Yang, Observation of stable Néel skyrmions in cobalt/palladium multilayers with Lorentz transmission electron microscopy, Nat. Commun. **8**, 14761 (2017).

[14] S. McVitie, S. Hughes, K. Fallon, S. McFadzean, D. McGrouther, M. Krajnak, W. Legrand, D. Maccariello, S. Collin, K. Garcia, N. Reyren, V. Cros, A. Fert, K. Zeissler, and C. H. Marrows, A transmission electron microscope study of Néel skyrmion magnetic textures in multilayer thin film systems with large interfacial chiral interaction, Sci. Rep. **8**, 5703 (2018).

[15] W. Jiang, X. Zhang, G. Yu, W. Zhang, X. Wang, M. Benjamin Jungfleisch, John E. Pearson, X. Cheng, O. Heinonen, K. L. Wang, Y. Zhou, A. Hoffmann, and Suzanne G. E. te Velthuis, Direct observation of the skyrmion Hall effect, Nat. Phys. **13**, 162 (2017).

[16] Z. Wang, M. Guo, H.-A. Zhou, L. Zhao, T. Xu, R. Tomasello, H. Bai, Y. Dong, S.-G. Je, W. Chao, H.-S. Han, S. Lee, K.-S. Lee, Y. Yao, W. Han, C. Song, H. Wu, M. Carpentieri, G. Finocchio, M.-Y. Im, S.-Z. Lin, and W. Jiang, Thermal generation, manipulation and thermoelectric detection of skyrmions, Nat. Electron. **3**, 672 (2020).

[17] S. Jaiswal, K. Litzius, I. Lemesh, F. Büttner, S. Finizio, J. Raabe, M. Weigand, K. Lee, J. Langer, B. Ocker, G. Jakob, G. S. D. Beach, and M. Kläui, Investigation of the Dzyaloshinskii-Moriya interaction and room temperature skyrmions in W/CoFeB/MgO thin films and microwires, Appl. Phys. Lett. **111**, 022409 (2017).

[18] T. Nozaki, Y. Jibiki, M. Goto, E. Tamura, T. Nozaki, H. Kubota, A. Fukushima, S. Yuasa, and Y. Suzuki, Brownian motion of skyrmion bubbles and its control by

voltage applications, Appl. Phys. Lett. **114**, 012402 (2019).
[19] G. Yu, A. Jenkins, X. Ma, S. A. Razavi, C. He, G. Yin, Q. Shao, Q. l. He, H. Wu, W. Li, W. Jiang, X. Han, X. Li, A. C. Bleszynski Jayich, P. K. Amiri, and K. L. Wang, Room-Temperature Skyrmions in an Antiferromagnet-Based Heterostructure, Nano Lett. **18**, 980 (2018).
[20] M. Bode, M. Heide, K. von Bergmann, P. Ferriani, S. Heinze, G. Bihlmayer, A. Kubetzka, O. Pietzsch, S. Blügel, and R. Wiesendanger, Chiral magnetic order at surfaces driven by inversion asymmetry, Nature **447**, 190 (2007).
[21] M. Heide, G. Bihlmayer, and S. Blügel, Dzyaloshinskii-Moriya interaction accounting for the orientation of magnetic domains in ultrathin films: Fe/W(110), Phys. Rev. B **78**, 140403 (2008).
[22] G. Chen, J. Zhu, A. Quesada, J. Li, A. T. N'Diaye, Y. Huo, T. P. Ma, Y. Chen, H. Y. Kwon, C. Won, Z. Q. Qiu, A. K. Schmid, and Y. Z. Wu, Novel Chiral Magnetic Domain Wall Structure in Fe/Ni/Cu(001) Films, Phys. Rev. Lett. **110**, 177204 (2013).
[23] G. Chen, A. Mascaraque, A. T. N'Diaye, and A. K. Schmid, Room temperature skyrmion ground state stabilized through interlayer exchange coupling, Appl. Phys. Lett. **106**, 242404 (2015).
[24] O. Boulle, J. Vogel, H. Yang, S. Pizzini, D. de Souza Chaves, A. Locatelli, T. O. Menteş, A. Sala, L. D. Buda-Prejbeanu, O. Klein, M. Belmeguenai, Y. Roussigné, A. Stashkevich, S. M. Chérif, L. Aballe, M. Foerster, M. Chshiev, S. Auffret, I. M. Miron, and G. Gaudin, Room-temperature chiral magnetic skyrmions in ultrathin magnetic nanostructures, Nat. Nanotechnol. **11**, 449 (2016).
[25] A. Soumyanarayanan, M. Raju, A. L. Gonzalez Oyarce, A. K. C. Tan, M.-Y. Im, A. P. Petrović, P. Ho, K. H. Khoo, M. Tran, C. K. Gan, F. Ernult, and C. Panagopoulos, Tunable room-temperature magnetic skyrmions in Ir/Fe/Co/Pt multilayers, Nat. Mater. **16**, 898 (2017).
[26] H. Wu, F. Groß, B. Dai, D. Lujan, S. A. Razavi, P. Zhang, Y. Liu, K. Sobotkiewich, J. Förster, M. Weigand, G. Schütz, X. Li, J. Gräfe, and K. L. Wang, Ferrimagnetic Skyrmions in Topological Insulator/Ferrimagnet Heterostructures, Adv. Mater. **32**, 2003380 (2020).
[27] G. Chen, T. Ma, A. T. N'Diaye, H. Kwon, C. Won, Y. Wu, and A. K. Schmid, Tailoring the chirality of magnetic domain walls by interface engineering, Nat. Commun. **4**, 2671 (2013).
[28] K. Zeissler, S. Finizio, K. Shahbazi, J. Massey, F. A. Ma' Mari, D. M. Bracher, A. Kleibert, M. C. Rosamond, E. H. Linfield, T. A. Moore, J. Raabe, G. Burnell, and C. H. Marrows, Discrete Hall resistivity contribution from Néel skyrmions in multilayer nanodiscs, Nat. Nanotechnol. **13**, 1161 (2018).
[29] A. Soumyanarayanan, N. Reyren, A. Fert, and C. Panagopoulos, Emergent phenomena induced by spin–orbit coupling at surfaces and interfaces, Nature **539**, 509 (2016).
[30] F. Hellman, A. Hoffmann, Y. Tserkovnyak, G. S. D. Beach, E. E. Fullerton, C. Leighton, A. H. MacDonald, D. C. Ralph, D. A. Arena, H. A. Dürr, P. Fischer, J. Grollier, J. P. Heremans, T. Jungwirth, A. V. Kimel, B. Koopmans, I. N. Krivorotov,

S. J. May, A. K. Petford-Long, J. M. Rondinelli, N. Samarth, I. K. Schuller, A. N. Slavin, M. D. Stiles, O. Tchernyshyov, A. Thiaville, and B. L. Zink, Interface-induced phenomena in magnetism, Rev. Mod. Phys. **89**, 025006 (2017).

[31] N. Nagaosa and Y. Tokura, Topological properties and dynamics of magnetic skyrmions, Nat. Nanotechnol. **8**, 899 (2013).

[32] M. J. Benitez, A. Hrabec, A. P. Mihai, T. A. Moore, G. Burnell, D. McGrouther, C. H. Marrows, and S. McVitie, Magnetic microscopy and topological stability of homochiral Néel domain walls in a Pt/Co/AlOx trilayer, Nat. Commun. **6**, 8957 (2015).

[33] W. Jiang, S. Zhang, X. Wang, C. Phatak, Q. Wang, W. Zhang, M. B. Jungfleisch, J. E. Pearson, Y. Liu, J. Zang, X. Cheng, A. Petford-Long, A. Hoffmann, and S. G. E. te Velthuis, Quantifying chiral exchange interaction for Neel-type skyrmions via Lorentz transmission electron microscopy, Phys. Rev. B **99**, 104402 (2019).

[34] A. Fert, V. Cros, and J. Sampaio, Skyrmions on the track, Nat. Nanotechnol. **8**, 152 (2013).

[35] J. Sampaio, V. Cros, S. Rohart, A. Thiaville, and A. Fert, Nucleation, stability and current-induced motion of isolated magnetic skyrmions in nanostructures, Nat. Nanotechnol. **8**, 839 (2013).

[36] X. Yu, M. Mostovoy, Y. Tokunaga, W. Zhang, K. Kimoto, Y. Matsui, Y. Kaneko, N. Nagaosa, and Y. Tokura, Magnetic stripes and skyrmions with helicity reversals, Proceedings of the National Academy of Sciences **109**, 8856 (2012).

[37] S. A. Montoya, S. Couture, J. J. Chess, J. C. T. Lee, N. Kent, D. Henze, S. K. Sinha, M. Y. Im, S. D. Kevan, P. Fischer, B. J. McMorran, V. Lomakin, S. Roy, and E. E. Fullerton, Tailoring magnetic energies to form dipole skyrmions and skyrmion lattices, Phys. Rev. B **95**, 024415 (2017).

[38] J. C. Loudon, A. C. Twitchett-Harrison, D. Cortés-Ortuño, M. T. Birch, L. A. Turnbull, A. Štefančič, F. Y. Ogrin, E. O. Burgos-Parra, N. Bukin, A. Laurenson, H. Popescu, M. Beg, O. Hovorka, H. Fangohr, P. A. Midgley, G. Balakrishnan, and P. D. Hatton, Do Images of Biskyrmions Show Type-II Bubbles?, Adv. Mater. **31**, 1806598 (2019).

[39] S. McVitie and M. Cushley, Quantitative Fresnel Lorentz microscopy and the transport of intensity equation, Ultramicroscopy **106**, 423 (2006).

[40] M. Krajnak, D. McGrouther, D. Maneuski, V. O. Shea, and S. McVitie, Pixelated detectors and improved efficiency for magnetic imaging in STEM differential phase contrast, Ultramicroscopy **165**, 42 (2016).

[41] M. He, L. Peng, Z. Zhu, G. Li, J. Cai, J. Li, H. Wei, L. Gu, S. Wang, T. Zhao, B. Shen, and Y. Zhang, Realization of zero-field skyrmions with high-density via electromagnetic manipulation in Pt/Co/Ta multilayers, Appl. Phys. Lett. **111**, 202403 (2017).

[42] K. X. Nguyen, E. Turgut, M. C. Cao, J. Glaser, Z. Chen, M. J. Stolt, S. Jin, G. D. Fuchs, and D. A. J. a. p. a. Muller, Disentangling magnetic and grain contrast in polycrystalline FeGe thin films using 4-D Lorentz Scanning Transmission Electron Microscopy, Preprint at arXiv:2001.06900, (2020).

[43] N. Romming, A. Kubetzka, C. Hanneken, K. von Bergmann, and R. Wiesendanger,

Field-Dependent Size and Shape of Single Magnetic Skyrmions, Phys. Rev. Lett. **114**, 177203 (2015).

[44] J. Lucassen, M. J. Meijer, O. Kurnosikov, H. J. M. Swagten, B. Koopmans, R. Lavrijsen, F. Kloodt-Twesten, R. Frömter, and R. A. Duine, Tuning Magnetic Chirality by Dipolar Interactions, Phys. Rev. Lett. **123**, 157201 (2019).

[45] K. v. Bergmann, A. Kubetzka, O. Pietzsch, and R. Wiesendanger, Interface-induced chiral domain walls, spin spirals and skyrmions revealed by spin-polarized scanning tunneling microscopy, J. Phys.: Condens. Matter **26**, 394002 (2014).

[46] M. J. Meijer, J. Lucassen, F. Kloodt-Twesten, R. Frömter, O. Kurnosikov, R. A. Duine, H. J. M. Swagten, B. Koopmans, and R. Lavrijsen, Magnetic Chirality Controlled by the Interlayer Exchange Interaction, Phys. Rev. Lett. **124**, 207203 (2020).

[47] See Supplementary Material at URL for additional information on technique and material comparisons, cross-sectional layer-structures, MTXM and LTEM images, micromagnetic simulation, magnetic flux from in-plane ($m_{x,y}$) and out-of-plane (m_z) components, simulated and experimental vertical component B_y and the magnitude |B|, and XAS and XMCD spectra at the Mn $L_{2,3}$ edge.

[48] T. Nagamiya, Triangular Spin Ordering in Mn_3Sn and Mn_3Ge, J. Phys. Soc. Jpn. **46**, 787 (1979).

[49] S. Nakatsuji, N. Kiyohara, and T. Higo, Large anomalous Hall effect in a non-collinear antiferromagnet at room temperature, Nature **527**, 212 (2015).

[50] M. Ikhlas, T. Tomita, T. Koretsune, M.-T. Suzuki, D. Nishio-Hamane, R. Arita, Y. Otani, and S. Nakatsuji, Large anomalous Nernst effect at room temperature in a chiral antiferromagnet, Nat. Phys. **13**, 1085 (2017).

[51] T. Higo, H. Man, D. B. Gopman, L. Wu, T. Koretsune, O. M. J. van 't Erve, Y. P. Kabanov, D. Rees, Y. Li, M.-T. Suzuki, S. Patankar, M. Ikhlas, C. L. Chien, R. Arita, R. D. Shull, J. Orenstein, and S. Nakatsuji, Large magneto-optical Kerr effect and imaging of magnetic octupole domains in an antiferromagnetic metal, Nature Photonics **12**, 73 (2018).

[52] M. Kimata, H. Chen, K. Kondou, S. Sugimoto, P. K. Muduli, M. Ikhlas, Y. Omori, T. Tomita, A. H. MacDonald, S. Nakatsuji, and Y. Otani, Magnetic and magnetic inverse spin Hall effects in a non-collinear antiferromagnet, Nature **565**, 627 (2019).

[53] K. Kuroda, T. Tomita, M. T. Suzuki, C. Bareille, A. A. Nugroho, P. Goswami, M. Ochi, M. Ikhlas, M. Nakayama, S. Akebi, R. Noguchi, R. Ishii, N. Inami, K. Ono, H. Kumigashira, A. Varykhalov, T. Muro, T. Koretsune, R. Arita, S. Shin, T. Kondo, and S. Nakatsuji, Evidence for magnetic Weyl fermions in a correlated metal, Nat. Mater. **16**, 1090 (2017).

[54] Y. Zhang, J. Železný, Y. Sun, J. van den Brink, and B. Yan, Spin Hall effect emerging from a noncollinear magnetic lattice without spin–orbit coupling, New Journal of Physics **20**, 073028 (2018).

[55] X. Li, C. Collignon, L. Xu, H. Zuo, A. Cavanna, U. Gennser, D. Mailly, B. Fauqué, L. Balents, Z. Zhu, and K. Behnia, Chiral domain walls of Mn3Sn and their

memory, Nat. Commun. **10**, 3021 (2019).
[56] H. Yang, Y. Sun, Y. Zhang, W.-J. Shi, S. S. P. Parkin, and B. Yan, Topological Weyl semimetals in the chiral antiferromagnetic materials Mn3Ge and Mn3Sn, New Journal of Physics **19**, 015008 (2017).
[57] R. Cardias, A. Bergman, A. Szilva, Y. O. Kvashnin, J. Fransson, A. B. Klautau, O. Eriksson, and L. Nordström, Dzyaloshinskii-Moriya interaction in absence of spin-orbit coupling, Preprint at arXiv:2003.04680, (2020).
[58] R. Yanes, J. Jackson, L. Udvardi, L. Szunyogh, and U. Nowak, Exchange Bias Driven by Dzyaloshinskii-Moriya Interactions, Phys. Rev. Lett. **111**, 217202 (2013).
[59] Y. Zhang, Y. Sun, H. Yang, J. Železný, S. P. P. Parkin, C. Felser, and B. Yan, Strong anisotropic anomalous Hall effect and spin Hall effect in the chiral antiferromagnetic compounds Mn_3X (X=Ge, Sn, Ga, Ir, Rh, and Pt), Phys. Rev. B **95**, 075128 (2017).
[60] S. Tomiyoshi and Y. Yamaguchi, Magnetic Structure and Weak Ferromagnetism of Mn3Sn Studied by Polarized Neutron Diffraction, J. Phys. Soc. Jpn. **51**, 2478 (1982).
[61] P. J. Brown, V. Nunez, F. Tasset, J. B. Forsyth, and P. Radhakrishna, Determination of the magnetic structure of Mn3Sn using generalized neutron polarization analysis, J. Phys.: Condens. Matter **2**, 9409 (1990).
[62] J. Finley and L. Liu, Spin-Orbit-Torque Efficiency in Compensated Ferrimagnetic Cobalt-Terbium Alloys, Phys. Rev. Appl. **6**, 054001 (2016).
[63] V. Puliafito, R. Khymyn, M. Carpentieri, B. Azzerboni, V. Tiberkevich, A. Slavin, and G. Finocchio, Micromagnetic modeling of terahertz oscillations in an antiferromagnetic material driven by the spin Hall effect, Phys. Rev. B **99**, 024405 (2019).
[64] L. Sánchez-Tejerina, V. Puliafito, P. Khalili Amiri, M. Carpentieri, and G. Finocchio, Dynamics of domain-wall motion driven by spin-orbit torque in antiferromagnets, Phys. Rev. B **101**, 014433 (2020).
[65] M. Binder, A. Weber, O. Mosendz, G. Woltersdorf, M. Izquierdo, I. Neudecker, J. R. Dahn, T. D. Hatchard, J. U. Thiele, C. H. Back, and M. R. Scheinfein, Magnetization dynamics of the ferrimagnet CoGd near the compensation of magnetization and angular momentum, Phys. Rev. B **74**, 134404 (2006).
[66] Y. Ogata, H. Chudo, M. Ono, K. Harii, M. Matsuo, S. Maekawa, and E. Saitoh, Gyroscopic g factor of rare earth metals, Appl. Phys. Lett. **110**, 072409 (2017).
[67] S. A. Siddiqui, J. Han, J. T. Finley, C. A. Ross, and L. Liu, Current-Induced Domain Wall Motion in a Compensated Ferrimagnet, Phys. Rev. Lett. **121**, 057701 (2018).
[68] S. McVitie, D. McGrouther, S. McFadzean, D. A. MacLaren, K. J. O'Shea, and M. J. Benitez, Aberration corrected Lorentz scanning transmission electron microscopy, Ultramicroscopy **152**, 57 (2015).
[69] M. Mansuripur, Computation of electron‐diffraction patterns in Lorentz electron microscopy of thin magnetic films, J. Appl. Phys. **69**, 5890 (1991).
[70] W. Legrand, J.-Y. Chauleau, D. Maccariello, N. Reyren, S. Collin, K.

Bouzehouane, N. Jaouen, V. Cros, and A. Fert, Hybrid chiral domain walls and skyrmions in magnetic multilayers, Sci. Adv. **4**, eaat0415 (2018).

[71] J. N. Chapman, P. E. Batson, E. M. Waddell, and R. P. Ferrier, The direct determination of magnetic domain wall profiles by differential phase contrast electron microscopy, Ultramicroscopy **3**, 203 (1978).

[72] J. Zhang, X. Zhang, H. Chen, Y. Guang, X. Zeng, G. Yu, S. Zhang, Y. Liu, J. Feng, Y. Zhao, Y. Zhou, X. Qiu, X. Han, Y. Peng, and X. Zhang, Formation and magnetic-field stability of magnetic dipole skyrmions and bubbles in a ferrimagnet, Appl. Phys. Lett. **116**, 142404 (2020).

[73] X. Ma, G. Yu, S. A. Razavi, S. S. Sasaki, X. Li, K. Hao, S. H. Tolbert, K. L. Wang, and X. Li, Dzyaloshinskii-Moriya Interaction across an Antiferromagnet-Ferromagnet Interface, Phys. Rev. Lett. **119**, 027202 (2017).

[74] Y. Guang, I. Bykova, Y. Liu, G. Yu, E. Goering, M. Weigand, J. Gräfe, S. K. Kim, J. Zhang, H. Zhang, Z. Yan, C. Wan, J. Feng, X. Wang, C. Guo, H. Wei, Y. Peng, Y. Tserkovnyak, X. Han, and G. Schütz, Creating zero-field skyrmions in exchange-biased multilayers through X-ray illumination, Nat. Commun. **11**, 949 (2020).

[75] G. Q. Yu, A. Jenkins, X. Ma, S. A. Razavi, C. L. He, G. Yin, Q. M. Shao, Q. L. He, H. Wu, W. J. Li, W. J. Jiang, X. F. Han, X. Q. Li, A. C. B. Jayich, P. K. Amiri, and K. L. Wang, Room-Temperature Skyrmions in an Antiferromagnet-Based Heterostructure, Nano Letters **18**, 980 (2018).

[76] H. Yang, A. Thiaville, S. Rohart, A. Fert, and M. Chshiev, Anatomy of Dzyaloshinskii-Moriya Interaction at Co/Pt Interfaces, Phys. Rev. Lett. **115**, 267210 (2015).

[77] H. Tsai, T. Higo, K. Kondou, T. Nomoto, A. Sakai, A. Kobayashi, T. Nakano, K. Yakushiji, R. Arita, S. Miwa, Y. Otani, and S. Nakatsuji, Electrical manipulation of a topological antiferromagnetic state, Nature **580**, 608 (2020).

[78] O. Gomonay, V. Baltz, A. Brataas, and Y. Tserkovnyak, Antiferromagnetic spin textures and dynamics, Nat. Phys. **14**, 213 (2018).

[79] T. Jungwirth, X. Marti, P. Wadley, and J. Wunderlich, Antiferromagnetic spintronics, Nat. Nanotechnol. **11**, 231 (2016).

Figures and Figure Captions

Figure 1. **Magnetic properties of the noncollinear antiferromagnetic Mn_3Sn.** Shown in Fig. A is the triangular AFM spin lattices of Mn_3Sn. The perpendicular magnetic hysteresis loop is shown in Fig. B. Shown in Fig. C is the room-temperature AHE observed in Mn_3Sn films grown on Al_2O_3 and SiO_2 substrates following the same procedure. Shown in Fig. D are the AHE loops measured in the CoTb/Mn_3Sn and CoTb/Ti/Mn_3Sn multilayers at room temperature.

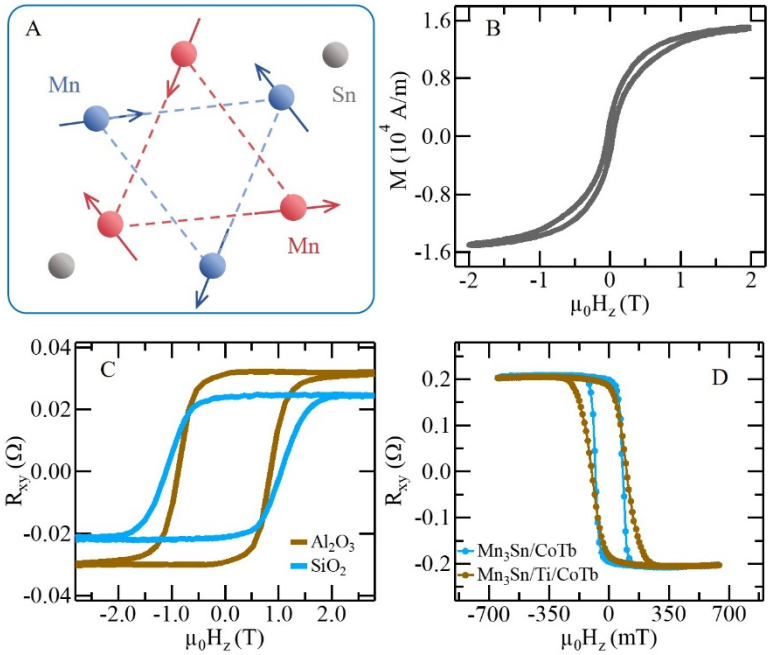

Figure 2. Structures and magnetic properties of the interfacially asymmetric multilayers. A. Schematic illustration of the asymmetric multilayers with an opposite stacking order. The numbers are the thickness of each layer in nanometer. B. Cross-sectional STEM imaging of $[Mn_3Sn/CoTb/Si_3N_4]_{20}$ multilayer. The scale bar is 40 nm. C and D. Out-of-plane and in-plane magnetic hysteresis loops for $[Mn_3Sn/CoTb/Si_3N_4]_{20}$ multilayer. E. The X-ray magnetic image at Co edge. F. Comparison between the experimentally determined sizes of skyrmion (square dot), and results from micromagnetic simulations (line).

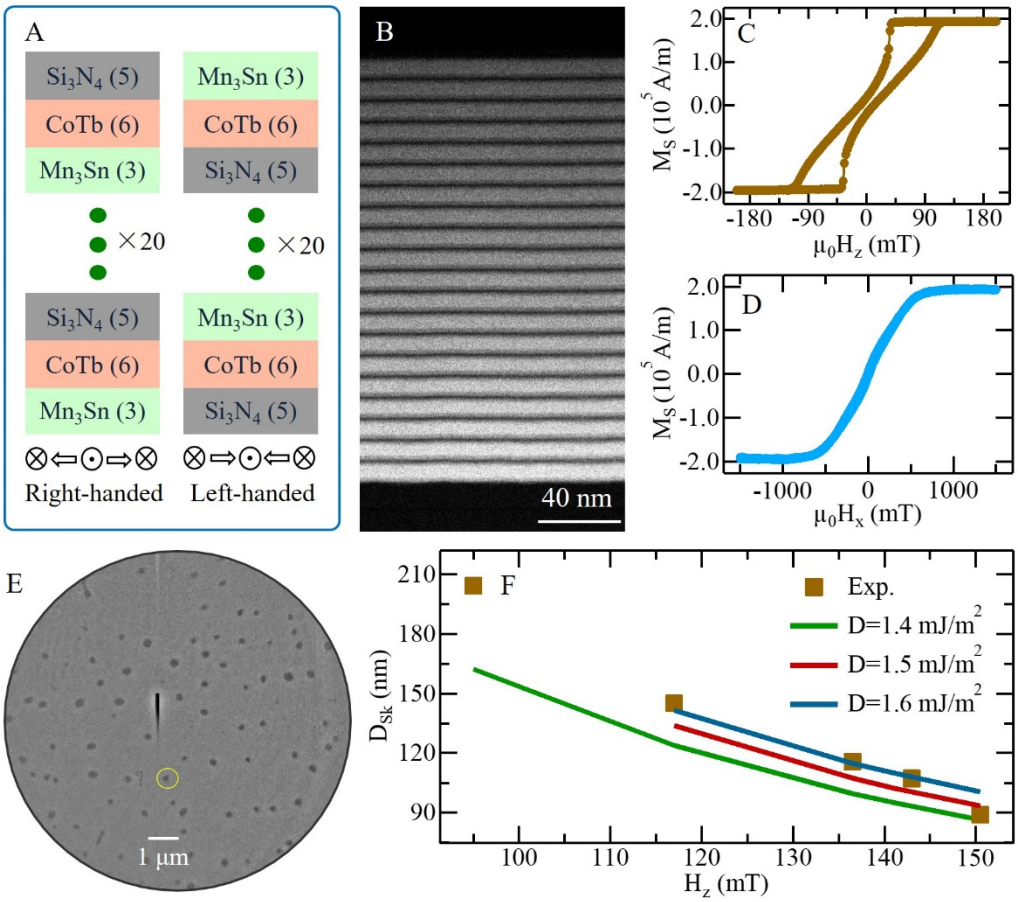

Figure 3. **LTEM images acquired at different magnetic fields and tilt angles.** LTEM images for magnetic multilayer $[Mn_3Sn/Co_{0.75}Tb_{0.25}/Si_3N_4]_{20}$ at (A) 0 mT and -20 degree tilt, (B) 0 mT and 0 degree tilt, (C) 0 mT and 20 degree tilt, (D) 104 mT and 20 degree tilt. LTEM images for the inverted multilayer acquired at (E) 0 mT and -20 degree tilt, (F) 0 mT and 0 degree tilt, (G) 0 mT and 20 degree tilt, (H) 104 mT and 20 degree tilt. The scale bar is 1 μm.

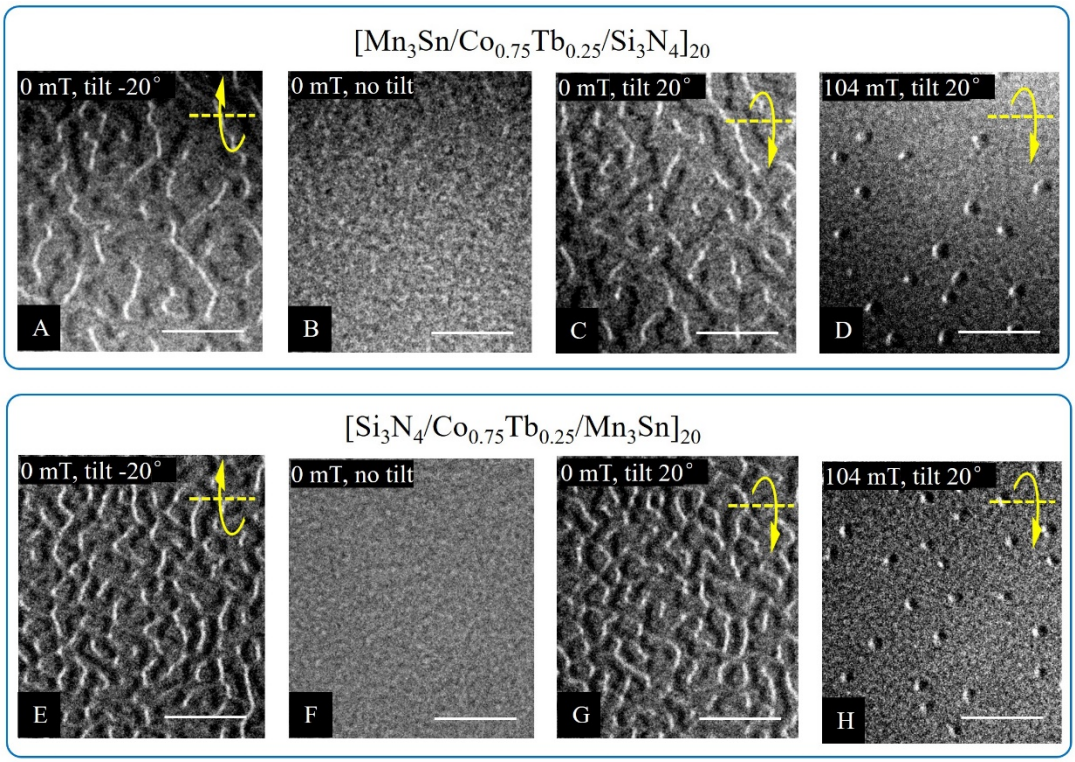

Figure 4. Identifying the spin chirality of Néel skyrmions with four-dimensional Lorentz STEM. A. The schematic illustration of the 4D LSTEM setup. B and C. Magnetic flux distributions for the right- and left-handed Néel skyrmions are shown in panels R1 & L1, while the horizontal component (B_x) of the simulated magnetic flux distribution at 20° tilt for the right- and left-handed Néel skyrmions are shown in panels R2 & L2, respectively. Experimentally determined magnetic fluxs of Néel skyrmions in $[Mn_3Sn/CoTb/Si_3N_4]_{20}$ and $[Si_3N_4/CoTb/Mn_3Sn]_{20}$ multilayers along horizontal (x)-direction are shown in panels R4 & L4. Panel R5 & L5 are the enlarged images of the selected skyrmions (red circles) in panels R4 & L4. Panel R3 & L3 are the simulated (R2 & L2) and experimental (R5 & L5) line profiles of magnetic flux magnitude (B_x) of the right-handed Néel skyrmion and left-handed Néel skyrmion along the direction marked with black and red arrows, respectively. Panel R6 & L6 are the experimental line profiles of the B_x of a few undistorted skyrmions in panel R4 & L4, respectively. All the images are plotted under the same x and y axes in A. The scale bars in Figs. B and C are 0.5 μm.

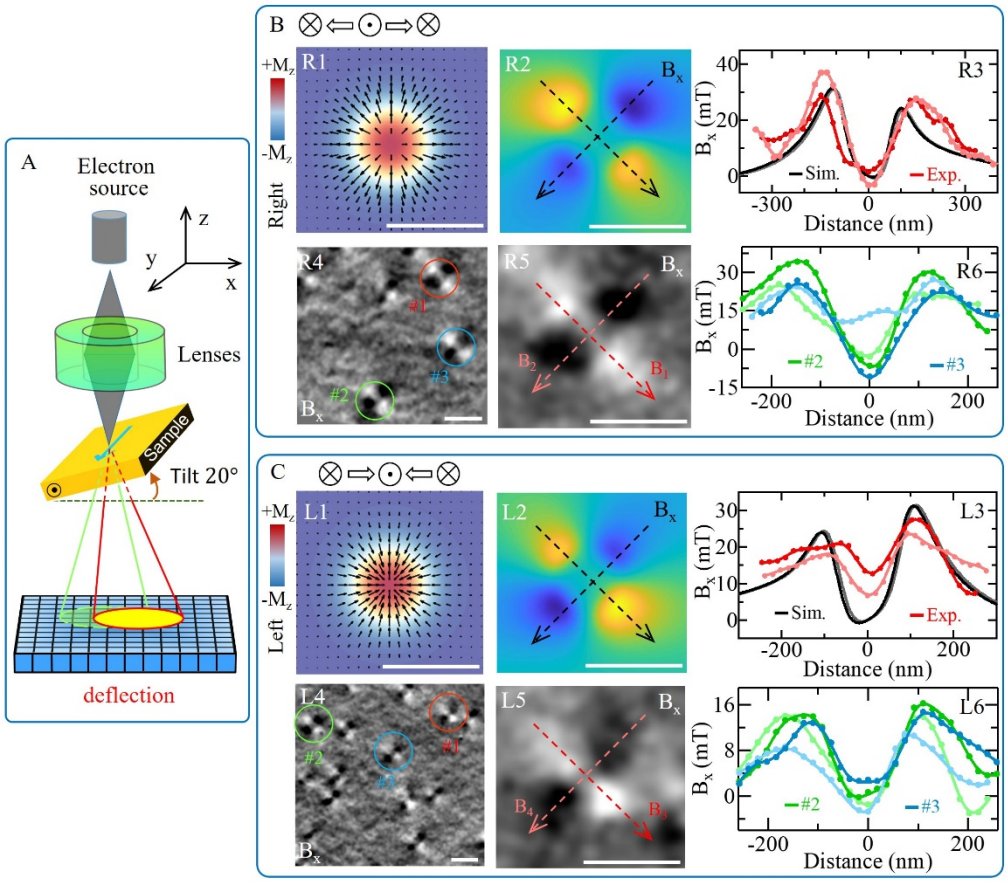

Figure 5. Chirality determination of FIM Néel skyrmions using XMCD-PEEM. A and B. The XMCD spectra measured at Co L_3-edge and Tb M_5-edge in the $[Mn_3Sn/CoTb/Si_3N_4]_{20}$ multilayer at $\mu_0 H_z = +2$ Tesla, respectively. Insets in A and B are the corresponding XMCD-PEEM images acquired at zero magnetic field. Scale bar is 1 μm. C. XMCD-PEEM image with an enhanced contrast at the Tb M_5-edge by averaging 500 images. The white arrow indicates the incident direction of the X-ray. Scale bar is 1 μm. D. Laterally averaged linescans of the magnetic contrast from the position marked locations in Fig. C. Dash lines indicate the XMCD brightness level of the corresponding out-of-plane domains, while additional dips/peaks between them correspond to in-plane magnetic moment of the chiral DWs. Inset is the schematic of the chiral spin texture. The blue color represents Tb while dark yellow corresponds to Co sublattices, respectively.